



# Numerical simulation on the effects of bubble size and internal structure on flow behavior in a DAF tank: A comparative study of CFD and CFD-PBM approach

Min Yang <sup>a,\*</sup>, David Fernandes del Pozo <sup>a</sup>, Elena Torfs <sup>a</sup>, Usman Rehman <sup>b</sup>, Dawei Yu <sup>a,c</sup>,  
Ingmar Nopens <sup>a,b</sup>

<sup>a</sup> BIOMATH, Department of Data Analysis and Mathematical Modelling, Ghent University, Coupure Links 653, 9000 Gent, Belgium

<sup>b</sup> AM-Team, Oktrooiplein 1, 9000 Gent, Belgium

<sup>c</sup> Research Center for Eco-Environmental Sciences, Chinese Academy of Sciences, 100085 Beijing, China



## ARTICLE INFO

### Keywords:

Population balance model  
Computational fluid dynamics  
Resource recovery  
Dissolved air flotation  
Optimization

## ABSTRACT

Although dissolved air flotation (DAF) plays a crucial role in wastewater treatment, fluid dynamics in the contact zone (CZ) of a DAF tank are still considered black-box processes, which hampers DAF's optimal design and operation. In this article, we perform a modeling study to further unravel the governing mechanisms occurring in a DAF tank. A computational fluid dynamics (CFD) model coupled with a generic population balance model (PBM) for the DAF system was developed in this work. CFD-PBM results showed that the eddy capture is the dominating mechanism for the bubble coalescence in the most volume of the CZ. Simultaneously, the velocity gradient mechanism and turbulent induced mechanism also play a key role in bubble coalescence in the regions with drastic flow transition and in the nozzle downstream. CFD-PBM simulations reveal that increasing the recirculation rate is better than increasing the volume fraction in the smaller recirculated flow to achieve higher bubble number density and smaller bubble size if the same amount of gas flow rate is injected. The baffle with proper transverse corrugate can equalize and reduce the total coalescence rate. By establishing a synergy between fluid dynamics and bubble size to achieve the best CZ efficiency, the generic CFD-PBM approach developed in this study has laid a solid basis for the optimal design and operation of DAF systems.

## 1. Introduction

Water scarcity is being recognized as a global threat to human activity and water reuse strategies deserve special attention as raised in EU water directives by the European Commission [1]. It is by no means possible to ensure access to water and sanitation for all by 2030, one of the seventeen UN sustainable development goals, without taking everlasting water reuse actions. Traditional wastewater treatment technologies such as conventional activated sludge deal with diluted wastes with diffuse emissions of methane and nutrients and are therefore not sustainable. The up-concentration of municipal wastewater followed by anaerobic digestion for the recovery of bioenergy allows for closing cycles. The core scientific problem in this approach lies in the revolution of the technology paradigm to address the up-concentration issue. DAF is such a separation technology that has the potential to address this issue [2–4]. Recently, research showed that the DAF generated A-sludge, with a concentration up to 47.1 g COD L<sup>-1</sup> and conversion efficiency

of CH<sub>4</sub> up to 68% when polymer and white water were added in the loop of the flocculator pipes, suppresses the need for further thickening before anaerobic digestion [5]. DAF is known for the efficiency of the removal of suspended particles from water with microbubbles. These microbubbles are generated when a mixture of air-saturated water experiences a sudden depressurization from high pressures (300–700 kPa) to atmospheric pressure. This sudden depressurization causes air desorption and produces microbubbles that adhere to the suspended particles in the bulk and float to the surface by means of buoyancy. As a result, a dense froth of attached bubbles and particles forms near the surface. A scraper then removes the froth layer, and the effluent with very little concentration of particles is drained out of the separation zone (SZ).

In general, the removal efficiency in DAF is a function of operating parameters (i.e., bubble size, hydraulic loading rate, reflux ratio, etc.) and reactor configuration (i.e., reactor design, baffle inclination and height, inlet and outlet configurations, nozzle structure, etc.). The design and operating parameters must be carefully considered such that

\* Corresponding author.

E-mail address: [yang.min@ugent.be](mailto:yang.min@ugent.be) (M. Yang).

the hydrodynamics in the contact and separation zones of the DAF is beneficial to achieve the desired bubble size and separation efficiency. The determination of these parameters is challenging and a better fundamental understanding of their roles and relationships is needed [6].

A commonly used technique for determining hydrodynamics of reactors is residence time distribution (RTD) analysis [7]. The earliest literature in DAF dates back to the work of [8]. They used the pulse-stimulus response test in a coaxial column to determine the degree of mixing in Peclet number and residence time in the CZ by RTD analysis. However, tracer tests cannot quantify the magnitudes of velocity locally and cannot represent the flow patterns clearly. Alternatively, mathematical modeling is a powerful tool that can be used to explore the physical phenomena occurring in a DAF system. Edzwald and his co-workers [6,9,10] proposed a so-called 'white water bubble blanket model (WWBB model)' based on the assumption of the prevalence of a plug flow in the CZ. The WWBB model considered bubbles in the white water blanket within the CZ as collectors of particles using the single collector efficiency approach to account for particle transport to the bubble interface [11]. The importance of the CZ was further proven by Fanaie et al. [12]. They investigated the effects of internal geometry on the fluid dynamics of DAF using the particle image velocimetry (PIV) technique. They observed flow circulations that occur in the upper part of the CZ, and as the height of the inlet baffle increased, the flow circulations became more intense. Theoretical models such as WWBB help understand the process better, but careful case-based revisions are required to accurately determine the optimal operating parameters and structural design due to questionable assumptions such as ideal plug flow and uniformity of bubble size and gas holdup.

CFD provides a powerful tool for detailed flow field investigations for the DAF system. Rodrigues and Béttiga [13] performed an evaluation of different approaches to the multiphase, turbulence and drag models, as well as different boundary conditions to model the surface of the DAF tank. The results indicated that the Eulerian approach and the realizable  $k-\epsilon$  turbulence model were the most adequate modeling to represent the flow behavior inside the DAF tank. The degassing boundary condition for free surface resulted in better results when compared with the non-slip wall condition. The results also indicate a low influence of the drag model on the hydrodynamics for the evaluated conditions. Lakghomi et al. [14] integrated a hetero-aggregation model into a pseudo-four-phase (water, air, particle, and aggregates) CFD model with particles described by a passive scalar under the Euler-Euler-Lagrange scheme. The CFD model demonstrated that the presence of stratified flow enhanced particle removal in the tank. A higher air fraction was needed at higher loading rates to achieve the same removal efficiency, and an optimum bubble size existed that increased with an increase in particle size. Bondelind et al. [15] applied single and two-phase numerical models to study the velocity field and gas holdup in a DAF tank. They demonstrated that the realizable  $k-\epsilon$  model was an acceptable compromise between the need to resolve the flow in the CZ correctly and the computational cost of the calculations. Chen et al. [16] employed Euler-Euler and Euler-Lagrange models to investigate the effect of microbubble sizes on the flow patterns and gas holdup. Modeling results indicated that Euler-Euler multiphase model made a better prediction of the air distribution in the SZ. The larger bubbles enhanced the stratified flow pattern for bubble diameters ranging from  $30\ \mu\text{m}$  to  $50\ \mu\text{m}$ . In a recent work from Satpathy et al. [17], flocs (particle phase) were introduced into the gas-liquid flow, and the CFD simulation results demonstrated that the flocs escaping through the outlet could be largely reduced by using a perforated tube for water extraction.

Most of these contributions focused mainly on the SZ analyzing the formation of stratified flow, which assumes a uniform bubble size distribution. Besides, the assumption of mono bubble size in these CFD models is quite different from the actual distributed behavior in the system and may lead to wrong conclusions. More attention needs to be paid to the CZ and particularly the baffle where bubble coalescence primarily occurs due to a higher level of turbulence and wall-bounded shear effects

[11]. Population balance models (PBMs) represent a powerful modeling framework for the description of the dynamics of bubble size distributions affected by local hydrodynamics in a DAF system [18]. PBMs can be used to develop new knowledge embedded in current CFD models to improve their predictive capability. Many researchers explored the bubble size distribution in flotation cells with CFD-PBM [19,20]. In such flotation cells, the effect of solid particle on bubble break-up and bubble coalescence rate in the flotation cells were investigated [21,22]. However, the PBM built for the flotation cells may not be suitable for DAF because the latter has a much smaller bubble size ( $10\text{--}200\ \mu\text{m}$ ) compared to those in flotation cells, which have a bubble size usually in the millimeter level [23]. The bubble coalescence mechanisms in the two flotation systems may be different due to the flow dynamics condition variation. Rodrigues et al. [24] incorporated population balance equations to simulate microbubble diameter distribution in a DAF tank. It showed that the coalescence model significantly impacted the gas phase's behavior in the white zone. However, their simulations indicated that the Luo model reduced in about 60% the air concentration in the positions evaluated compared with the Turbulent coalescence model, indicating a need for further investigation of the bubble coalescence mechanisms in the DAF system.

Chen et al. [23] implemented a CFD-PBM model in a CZ of a DAF tank. It was found that the PBM considering only the coalescence due to the eddy-capture and velocity gradient could accurately predict the bubble diameter and its size distribution. However, the presumption that the Kolmogorov microscale in the whole system was larger than the bubble sizes may not necessarily be true. As a result, the mechanisms governing the bubble coalescence in DAF system need to be further explored. Besides, the air was injected downwards instead of spraying towards the baffle, so the effects of the baffle on the flow behavior and on the bubble coalescence were insignificant and were not investigated in their study [23]. It is necessary to further develop a generic CFD-PBM model for a more realistic DAF system, especially when the effects of different configurations and various operations on bubble size and fluid dynamics need to be investigated.

Therefore, this study aims to develop a generic PBM and to couple it with CFD for the prediction of flow behavior in a realistic DAF system. CFD simulations without PBM were first carried out to predict the flow dynamics in a DAF pilot plant under different mono microbubble sizes [25]. CFD-PBM simulations were then performed to better understand and predict the interaction between flow dynamics and bubble size distribution dynamics to provide a complete model basis for DAF structure and operation optimization.

## 2. Materials and methods

### 2.1. DAF set-up

The pilot DAF tank employed in this study is taken from Lundh et al. [26] (Fig. 1). Information about the DAF configuration and operation used in this study is listed in Table 1 and Table 2, respectively. The original baffle and longer baffle were adapted from Lundh et al. [26], while the corrugated (semicircular, triploid) baffle and the longer baffle are proposed in this study. Case M18 and case M19 have been numbered previously by Lundh et al. [25], and that notation (M18, M19) is kept throughout the paper for transparency. Case M0 is proposed in this study to understand better the effect of the recycling rate and air intake on the bubble size distribution.

The sliced plane at  $x = 0.19\text{ m}$  and  $y = 0.35\text{ m}$  are used to visualize the CZ's flow behavior and the overall DAF tank, respectively (Fig. 1). In this DAF system, the main water stream enters the inlet zone (IZ) at the inlet and is mixed with the recycle flow injected from the needle valves in the CZ. The clear water is discharged through two outlet pipes at the bottom of the tank in the SZ. The right side shows the shape of the original plane baffle (OP) (a), longer plane baffle (LP) (b), single semicircular corrugated baffle (SSC) (c), single trapezoidal corrugated

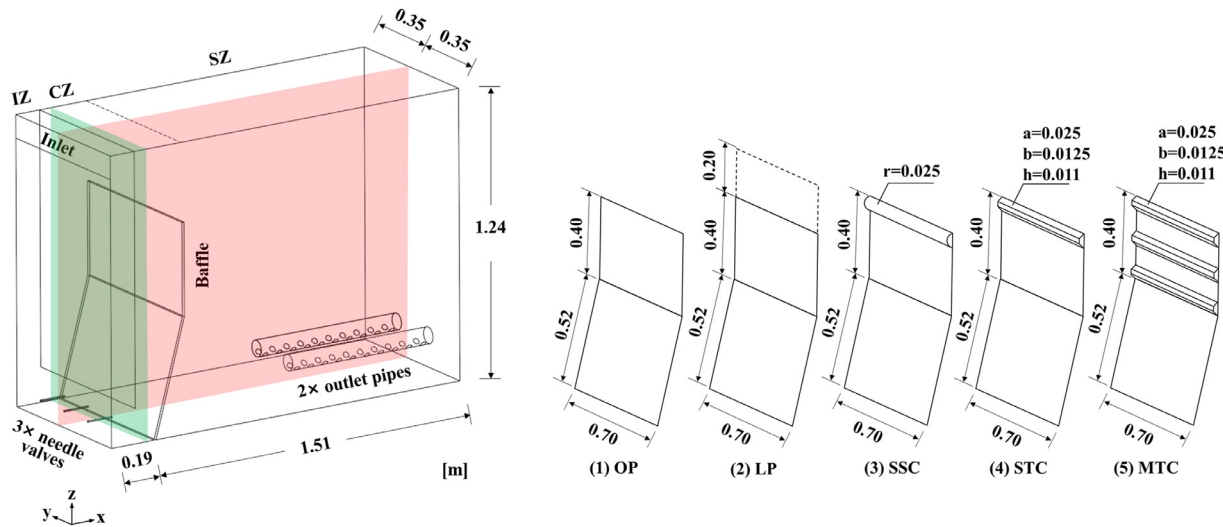


**Fig. 1.** The geometry of a pilot DAF tank on the left in which the experiments were carried out by Lundh et al. [26] (the green plane and the red plane represent cross-sections:  $x = 0.19$  m, and  $y = 0.35$  m, respectively) and the baffle configurations on the right (a, b, h represent the side length of the upper length, bottom length and height of the trapezoid, and r represents the radius of the half-cylinder) studied in this study.

**Table 1**  
Configuration information of the DAF tank used for the simulation (units: mm) [25,26].

Item	Size/form
Contact zone	220/350(L) $\times$ 1240(H) $\times$ 700(W)
Separation zone	1350(L) $\times$ 1240(H) $\times$ 700(W)
Inlet	190 (H) $\times$ 340 (W)
Needle valves (Diameter, number)	5.0, 3
Outlet pipe (Diameter, number)	70, 2
Holes on each outlet pipe (Diameter, number)	25, 2 $\times$ 10
Baffle shape	original, longer, corrugated (semicircular, triploid)

**Table 2**  
Operating conditions of the DAF process for the simulations.

Number	Flowrate, m <sup>3</sup> /h	Recycle rate, %	Surface loading, m/h	v <sub>water,in</sub> , m/s	v <sub>mixture,rec</sub> , m/s	c <sub>air,rec</sub>	Air intake, m <sup>3</sup> /s
M18	10	5	9.5	0.04	2.36	4.7%	6.53e <sup>-6</sup>
M19	10	10	10	0.04	4.72	5.8%	1.61e <sup>-5</sup>
M0	10	5	9.5	0.04	2.36	11.6%	1.61e <sup>-5</sup>

baffle (STC) (d), and multiple trapezoidal corrugated baffle (MTC) (e), which were the configurations used in this study.

Here, we validated our simulations with experimental data obtained by Lundh et al. [25,26] in a pilot-scale DAF tank, in which an Acoustic Doppler Velocimeter (ADV, Nortek A/S) was used for measuring 3-D mean water velocities. The air concentration profile plotted as a function of the tank height at  $x = 650$  mm, 1050 mm, and 1350 mm against the vertical axis is measured by Lundh [26]. However, the interpretation of the experimental results is not a trivial task. For example, when using ADV, it will interfere with the flow and reduce the magnitude of the velocity measurements. The decrease in velocity magnitude is explained by the presence of air bubbles interfering with the equipment. The air content in the tank was measured with a calibrated turbidity meter (Surface Scatter 6, Hach) and calibrated with a syringe method in their study [25,26]. A small hose was located at the desired location, and water was drawn to the turbidity meter, where the bubble concentration was measured as turbidity (NTU). However, the authors claimed that the exact bubble content in the measuring point could not be determined but only indicate a trend of bubble content [26]. The difficulties in retrieving reliable information from experiments illustrate the necessity of using additional tools like CFD to examine the DAF system. Indeed, when setting up a numerical model, data from measurements is needed to reduce uncertainty both in terms of geometry and

model parameters. However, as pointed out by Bondelind et al. [15], the measuring techniques struggle with the problems mentioned above, providing data that only allows qualitative comparison between numerical predictions and experimental measurements. As for the bubble size distribution, Lundh and his co-workers did not supply BSD data for this pilot-scale DAF. The experimental data of bubble size distribution measured in a similar DAF system (with a comparable CZ size and operating condition as M18) (Chen et al., 2019) was tested and used to validate the generic PBM model developed in this study. The bubble classes and initial fraction in the nozzle inlet are presented in Table 3 (Chen et al., 2019).

## 2.2. CFD model settings for gas–liquid flow

Steady-state gas-liquid two phase flow simulations were carried out considering that the experimental data were collected in a DAF tank operated without any particles steadily [25]. The pressure-based solver was used to solve the three-dimensional two-phase mass and momentum conservation equations. Each phase is governed by respective mass and momentum conservation equations within the Euler-Euler (E-E) multiphase framework [27]. The drag force is considered to be the contribution to interphase momentum transfer described by Schiller-Naumann

**Table 3**

The bubble classes and their initial volume of fraction in the nozzle inlet used in this study [23].

Bubble class	bin15	bin14	bin13	bin12	bin11	bin10	bin9	bin8
Size ( $\mu\text{m}$ )	20.0	23.0	26.4	30.3	34.8	40.0	45.9	52.8
Fraction	3.8	9.4	24.8	22.7	20.1	9.7	6.6	1.4
Bubble class	bin7	bin6	bin5	bin4	bin3	bin2	bin1	bin0
Size ( $\mu\text{m}$ )	60.6	69.6	80.0	91.9	105.6	121.3	139.3	160.0
Fraction	1.5	0.0	0.0	0.0	0.0	0.0	0.0	0.0

model [27]. The turbulent dispersion force, acting as a turbulent diffusion in dispersed flows, arises from averaging the interphase drag term and is calculated according to the Favre Average Drag (FAD) model proposed by Burns et al. [28]. Bubbles tend to get caught up in continuous phase turbulent eddies and hence be carried from regions of high concentration to areas of low concentration. The dispersion force exerts a smoothing effect on the gas volume fraction profile. The FAD model addresses this phenomenon and considers the influence of bubble size on the bubble dispersion, making it more suitable for systems with different bubble sizes. As the flow behavior in the CZ is the main interest in this study, the needle injection is very important for the flow development in this zone and the rotation flow in the CZ is likely to be formed. So the realizable  $k - \epsilon$  model was chosen in this study, with the flow near the walls resolved using non-equilibrium wall functions [15]. A velocity inlet boundary was applied for the feed water inlet and air/water mixture needle inlet (Table 2). A degassing boundary condition was specified for the water-air surface at the top of the DAF tank. Wall surfaces and baffles were treated as no slip walls, where the roughness constant and the roughness height at the no slip walls were set as 0.5 and 0.0, respectively. Residuals criteria of  $10^{-4}$  was used for convergence of all flow variables. Flow velocity and gas holdup at the outlet were monitored to ensure the simulation reached a steady state.

### 2.3. Residence time model

RTDs used as post-processing tools, together with 3D CFD visualizations, are usually applied to characterize the hydrodynamic characteristics of virtual reactors (reactors simulated by CFD). In this study, the residence time is obtained by solving the steady-state convection-diffusion equation with a passive scalar field upon obtaining the fully converged flow field.

The transport of a passive scalar through an incompressible fluid is described as:

$$\frac{\partial}{\partial t}(\rho\phi) + \frac{\partial}{\partial x_i} \left( \rho u_i \phi - \Gamma_\phi \frac{\partial \phi}{\partial x_i} \right) = S_\phi \quad (1)$$

where  $\phi$  is an arbitrary scalar such as time,  $\Gamma_\phi$  is the diffusion coefficient of  $\phi$ , and  $S_\phi$  is a source term.

The diffusion term is removed, given there exists neglectable diffusion between the tracer and the background fluid. By specifying the source term ( $S_\phi$ ) to be the density ( $\rho$ ) of the fluid phase in which the scalar is added, then the residence time can be obtained by solving the convection term under steady-state as:

$$\frac{\partial}{\partial x_i}(u_i \phi) = 1 \quad (2)$$

Where  $\phi$  becomes the residence time here, which is introduced as a user-defined scalar (UDS).

In a steady-state CFD simulation, the residence time (and other variables, such as velocity field, pressure, the volume fraction of gas) can be obtained at any point in the space of the discretized geometry. Large amounts of information (usually millions of velocity vectors) cannot quickly gain insight into the overall mixing that occurs in the process, nor does it allow for easy comparison between geometries. A large number of results of local magnitudes of fluid dynamical variables, however, will enable the calculation of the Cumulative Variables Distributions

representative of the reactor homogeneity, also referred to as "Rehmann-Nopens (RN) curves" [29,30]. Typically, steep RN-curves indicate homogeneous zones in the variable, while less steep ones indicate a higher degree of heterogeneity. This way, the comparison of the different scenarios becomes straightforward by merely looking at the shape of the RN-curves.

### 2.4. Population balance model

To simulate the bubble breakup and coalescence process in a bubble-water system, one of the promising approaches is to use population balance models (PBMs), which describe the variation in a given population property over space and time in a velocity field. Specifically, the application of PBM in the DAF system is to determine the bubble size distribution over space and time and how this distribution changes due to the breakup and coalescence processes. As pointed out by previous studies, there is little chance for a bubble to break up further in a DAF tank, where the turbulent intensity is expected to be small [23,31]. Bubble breakage events occur as a result of the interaction between a turbulent eddy and a bubble. Only if the energy supplied by the eddy is greater than the increase in surface energy needed to create two bubbles, then the collision can result in breakage [32,33]. As a result, a generally accepted assumption is that only if the eddy size is similar or smaller than the bubble may lead the bubble to break. Apart from the lumen of the nozzles, turbulent eddies size characterized by the Kolmogorov length,  $\eta$  are of 0.2 mm - 5 mm in the DAF tank in this study, which turns out to be too large to consider breakage of microbubbles (20 - 200  $\mu\text{m}$ ). This study found that with or without the inclusion of bubble breakage kernels did not make a difference to the bubble size distributions for various operations employed in this study. So the breakage kernel was not further considered. This simplifies the analysis since the population balance equation only needs to consider the bubble coalescence and it is therefore defined as,

$$0 = \underbrace{\frac{1}{2} \int_0^V a(V - V', V') n(V - V') n(V', t) dV'}_{\text{Birth due to Aggregation}} - \underbrace{\int_0^\infty a(V, V') n(V) n(V') dV'}_{\text{Death due to Aggregation}} \quad (3)$$

Where  $V$  is the volume of a bubble being aggregated from two smaller bubbles with a size of  $V - V'$  and  $V'$  in a bubble birth event.  $V$  can also be the volume of a particle being aggregated with a bubble with a size of  $V'$  to form a new bubble with a volume of  $V + V'$  in a particle death event.  $n(V')$  is the number density function of bubbles with a volume of  $V'$ .

The  $a(V - V', V')$  term is the aggregation kernel and it is usually denoted as  $\Gamma_{ij}$ , which is defined as a product of two quantities:  $\omega_{ij}$ , is the frequency of collisions between particles of size  $d_i$  and particles of size  $d_j$ , and  $\lambda_{ij}$ , is the "efficiency of aggregation" (that is, the probability of particles of size  $d_i$  coalescing with particles of size  $d_j$ ), and it can be expressed as

$$\underbrace{\Gamma_{i,j}}_{\text{coalescence rate}} = \underbrace{\omega_{i,j}}_{\text{coalescence frequency}} \cdot \underbrace{\lambda_{i,j}}_{\text{coalescence efficiency}} \quad (4)$$

The collision frequency between two bubbles is modeled in analogy to gas kinetic theory. It can be approximated as the volume swept by the

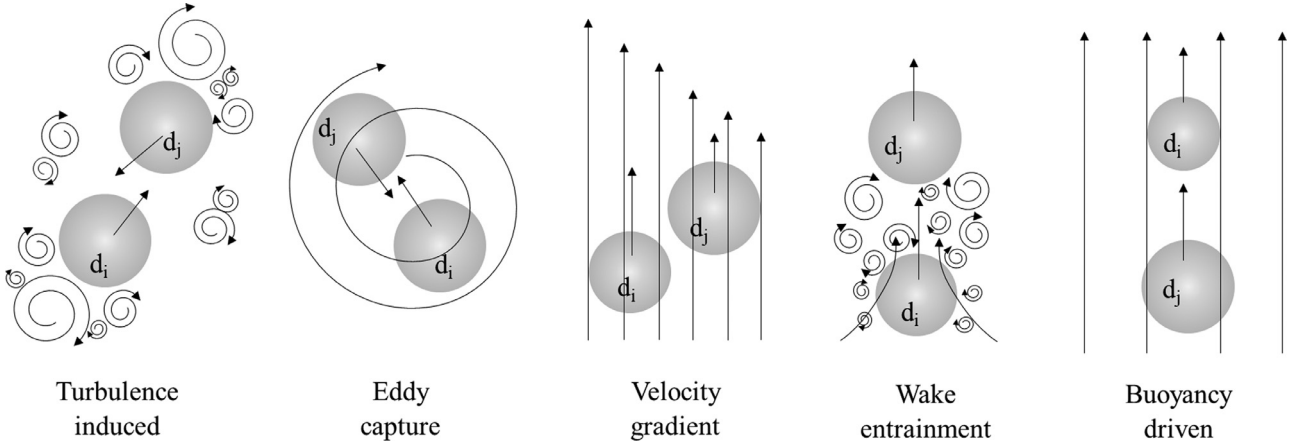


Fig. 2. Mechanisms leading to bubble collision in a turbulent flow.

bubbles in unit time, i.e.,

$$\omega_{i,j} = A_{i,j} \cdot u_{rel} \quad (5)$$

where  $u_{rel}$  is the approach velocity between the bubbles and  $A_{i,j}$  is the effective cross-sectional area for a collision. These quantities are determined in different ways for each collision mechanism, as will be discussed in the following, i.e., Eq. (6) to Eq. (19).

The film drainage model proposed by Shinnar and Church [34] was usually used to describe the bubble coalescence process. Shinnar and Church state that after the collision, two bubbles may cohere together and be prevented from coalescing by a thin film of liquid trapped between them. Attractive forces between them drive the film to drain out until it collapses, and coalescence follows. Numerous bubble coalescence kernels following this theory are reported in the literature [35,36]. Normally, five mechanisms of collisions are included, namely, the collisions due to turbulent fluctuation, eddy capture, Buoyancy driven, wake entrainment, and velocity gradient (Fig. 2).

However, not all of them are of importance to a rigid bubble system such as DAF. The wake entrainment needs to be considered only for large bubbles due to the fact that the frequency of the bubble collision induced by wake entrainment is directly proportional to the wake volume and inversely proportional to the average distance between two bubbles [37]. The microbubbles in a DAF have a very small wake volume, and due to the low gas holdup, the average distance between the microbubbles is relatively large [20]. As a result, wake entrainment hardly contributes to bubble coalescence in the CZ [23]. The buoyancy-induced bubble coalescence, which assumes that a collision can only happen if the faster bubble approaches the slower one from below in an upward flow. But the relative velocity of bubbles to water is very small in a DAF system. It's difficult for a buoyancy-induced bubble coalescence to happen [38]. Microbubbles in large part of the DAF systems safely fall in the range of viscous regime (Section 3.3), which means that the eddies are much larger than the bubble size and can only capture and transport groups of bubbles without leading to significant relative turbulence motion. As a result, eddy capture coalescence forces need to be included for microbubbles. The turbulent induced coalescence is normally the most significant mechanism in the inertial collision regime such as bubble columns with bubble sizes of several millimeters [39]. Inertial collision regime could also occur at the narrow downstream of the recycle nozzle, which introduces a high flow speed of gas-liquid mixture and a high turbulent eddy dissipation rate. The eddies have a large chance to be smaller than the bubble size, and the turbulent induced coalescence rather than the eddy capture coalescence should be applied in the nozzle downstream region.

In summary, the eddy capture, the turbulent induced and the velocity gradient bubble coalescence mechanisms were employed in the PBM

in this work. These mechanisms and the evidence to choose them are further described in the following sections.

#### 2.4.1. Eddy-capture-induced coalescence

The collision between bubbles, which are much smaller than the Kolmogorov length scale, is assumed to be controlled by viscous forces. The coalescence rate  $\Gamma_{i,j}^E$  is obtained by analogy to Eq. (6):

$$\Gamma_{i,j}^E = \omega_{i,j}^E \cdot \lambda_{i,j}^E = 0.5 \frac{\pi}{4} (d_i + d_j)^2 \underbrace{\left[ \frac{0.5}{\pi} (d_i + d_j) \dot{\gamma} \right]}_{u_{rel, eddy}} \cdot \lambda_{i,j}^{viscous} (d_i + d_j \leq \eta) \quad (6)$$

The characteristic strain rate of the flow in the smallest eddies,  $\dot{\gamma}$ , can be derived from the Kolmogorov scales as,

$$\dot{\gamma} = \sqrt{\varepsilon/\nu} \quad (7)$$

Where  $\nu$  is the kinematic viscosity,  $\varepsilon$  is the turbulent eddy dissipation rate.

The film drainage model determines the coalescence efficiency from two characteristic time scales, i.e., the contact time  $\tau_{c_{i,j}}$  and the drainage time  $t_{c_{i,j}}$ , where the latter is the time required for the intervening film between the bubbles to thin down to a critical thickness [35,40]. The coalescence efficiency in line with this theory thus can be expressed as

$$\lambda_{i,j}^{viscous} = \exp\left(-\frac{t_{c_{i,j}}}{\tau_{c_{i,j}}}\right) \quad (8)$$

For the non-deformable rigid bubbles like microbubbles in the DAF system, the drainage time was derived by Chesters [36] by using the Poiseuille relation,

$$t_{c_{i,j}} \approx \frac{1}{8\dot{\gamma}} \ln\left(\frac{3}{4} Fl\right) \quad (9)$$

Where  $Fl$  is the flow number and is calculated by

$$Fl = 6\pi\mu_L \dot{\gamma} r_{i,j}^3 / A \quad (10)$$

Where  $r_{i,j}$  representing the equivalent radius for two cohering rigid bubbles with diameters of  $d_i$  and  $d_j$ , respectively,

$$r_{i,j} = \frac{d_i d_j}{d_i + d_j} \quad (11)$$

$A$  is the Hamaker constant representing the strength of van der Waals interactions between macroscopic bodies. For air-water interfaces, its value is  $A \approx 3.7 \times 10^{-20} J$ .

And the contact time in Eq. (8) can be calculated as,

$$\tau_{c_{i,j}} \approx \frac{1}{\dot{\gamma}} \quad (12)$$

Combining Eq. (8), Eq. (9), and Eq. (12), the coalescence efficiency in the viscous regime can then be expressed as

$$\lambda_{i,j}^{viscous} = c_1 \left( 9\pi\mu_L \dot{r}_{i,j}^3 / 2A \right)^{-1/8} \quad (13)$$

The value of  $c_1$  is of order unity according to Chesters [36] and thus, it was set to be 1.0 in this work.

#### 2.4.2. Turbulent-induced coalescence

For a random collision caused by turbulent fluctuations, the collision frequency is approximated as the volume swept by two bubbles with an approach velocity  $u_{rel, turb}$  in unit time. In analogous to gas kinetic theory [32], the collision frequency between two single bubbles can be expressed as:

$$\Gamma_{i,j}^T = \omega_{i,j}^T \cdot \lambda_{i,j}^T = \frac{\pi}{4} (d_i + d_j)^2 \underbrace{\left[ \sqrt{2} \left( d_i^{2/3} + d_j^{2/3} \right)^{1/2} \varepsilon_i^{1/3} \right]}_{u_{rel, turb}} \cdot \lambda_{i,j}^{inertial} \quad (d_i + d_j > \eta) \quad (14)$$

For an inertial collision, the coalescence efficiency is estimated as (Chesters, 1991):

$$\lambda_{i,j}^{inertial} = \exp \left( -c_{eff} W e_{ij, max}^{0.5} \right) \quad (d_i + d_j > \eta) \quad (15)$$

Where the constant  $c_{eff}$  has a suggested value of 5.0 [38], which has also been used in this work. To consider the competing effect of various mechanisms (i.e., velocity gradient induced and turbulent induced) in this study, the maximum Weber number in Eq. (15) is expressed as [38]:

$$W e_{ij, max} = \frac{\rho_l d_{i,j}}{\sigma} \max(u_{rel, turb}, u_{rel, shear})^2 \quad (d_i + d_j > \eta) \quad (16)$$

#### 2.4.3. Velocity gradient-induced coalescence

According to Liao [38], the rate of the collision induced by the velocity gradient can be calculated by

$$\Gamma_{i,j}^S = \omega_{i,j}^S \cdot \lambda_{i,j}^S = 0.5 \frac{\pi}{4} (d_i + d_j)^2 \underbrace{\left[ \frac{0.5}{\pi} (d_i + d_j) \dot{\gamma}_b \right]}_{u_{rel, shear}} \cdot \lambda_{i,j}^{eff} \quad (17)$$

with the effective coalescence efficiency given by:

$$\lambda_{i,j}^{eff} = \begin{cases} \lambda_{i,j}^{inertial} & (d_i + d_j > \eta) \\ \lambda_{i,j}^{viscous} & (d_i + d_j \leq \eta) \end{cases} \quad (18)$$

with  $\dot{\gamma}_b$  the shear strain rate of the bulk flow to represent the velocity gradient for generality:

$$\dot{\gamma}_b = \left[ \begin{array}{l} 2 \left( \frac{\partial u_l}{\partial x} \right)^2 + 2 \left( \frac{\partial v_l}{\partial y} \right)^2 + 2 \left( \frac{\partial w_l}{\partial z} \right)^2 + \\ \left( \frac{\partial u_l}{\partial y} + \frac{\partial v_l}{\partial x} \right)^2 + \left( \frac{\partial u_l}{\partial z} + \frac{\partial w_l}{\partial x} \right)^2 + \left( \frac{\partial u_l}{\partial z} + \frac{\partial w_l}{\partial y} \right)^2 \end{array} \right]^{1/2} \quad (19)$$

#### 2.4.3. Solution methods

The population balance equation can be solved by different methods such as the discrete method and the quadrature method of moments (QMOM) [41]. The discrete method is based on representing the continuous bubble size distribution (BSD) in terms of a set of discrete size classes or bins. The advantages of this method are having robust numeric and that it gives the BSD directly. The disadvantages are that the bins must be defined *a priori* and that a large number of classes may be required [42,43]. The QMOM provides an alternative to the discrete method when aggregation quantities, rather than an exact BSD, are desired [44]. Its advantages are fewer variables (typically only six or eight moments) and a dynamic calculation of the size bins. The disadvantages are that the number of abscissas may not be adequate to describe the BSD and that solving the Product-Difference algorithm may be time-consuming.

In this study, the range of bubble sizes in the nozzle inlet is divided into 16 classes and is known as *a priori*, which was taken from a similar study from Chen [23] (Table 3). As a result, the discrete method

was employed to resolve the population balance equation in this study. The mean bubble diameter was represented by the Sauter diameter,  $d_{32}$ , which can be calculated by the number density function  $n_i$  and bubble size  $d_i$  in each class.

$$d_{32} = \frac{\sum n_i d_i^3}{\sum n_i d_i^2} \quad (20)$$

With the input of the Sauter diameter calculated by the PBM, CFD models related to bubble sizes, such as interphase force and multiphase model, can be adjusted in each iteration accordingly. And the hydrodynamic results computed by the CFD model, such as the turbulent eddy dissipation and velocity, are used to update the coalescence frequency and efficiency in the PBM calculation. This process is repeated until the calculation converges. To couple PBM with CFD, a User Defined Function (UDF) was compiled and hooked to include the bubble coalescence process affected by the flow dynamics, and vice versa (Fig. 3). Concerned variables such as coalescence frequency and coalescence efficiency were extracted and visualized through the usage of User Defined Memory (UDM).

## 3. Results and discussion

### 3.1. Model validation

A grid independence study has been performed on the DAF with the original baffle configuration. To accurately evaluate the numerical uncertainties in the computational results, the concept of grid convergence index (GCI) was adopted using the three grid levels (Fig. S1 & Table S1). The CFD simulations successfully predicted the form and magnitude of the stratified flow occurring in the SZ. It also captured the trends compared to the experimental measurements as the air content increases along with height (Fig. 4). In addition, the CFD-PBM simulations were found to fit the experimental data quite well as presented in Section 3.4 (Fig. 10). This shows the CFD and CFD-PBM model developed in this work are sufficient for the simulation and optimization of flow dynamics in a DAF. However, like CFD simulations from other researchers [15], this study did not capture the sudden decrease of air below  $z = 0.6$  m, as indicated by the measurements [45]. This mismatch may be attributed to modeling inaccuracies from the turbulence model and the limitations of the measuring technique, as pointed out by Bondelind et al. [15]. As for the turbulence model, the other possibilities, such as SST k- $\omega$  would have had the same problem in predicting free shear flow as fully turbulent. There are more advanced models, such as the large eddy simulations (LES), that would capture many unsteady states, large-scale effects, and quasi-ordered structures that would appear in non-equilibrium processes, which the RANS method cannot resolve. But it requires substantially finer meshes than those typically used for RANS calculations. Because this study focuses on the CZ with sufficient turbulence, the RANS turbulence model used (i.e., the realizable k- $\epsilon$ ) is deemed to be a reasonable choice to maintain a balance between accuracy and efficiency. Nevertheless, it is needed for future work to put experimental efforts with advanced experimental tools such as PIV and X-Ray for the validation of CFD simulations of full scale DAF systems [46].

### 3.2. The effect of bubble size on the contact zone efficiency

CFD simulations without PBM were carried out to predict the flow dynamics under different mono microbubble sizes in this section. The effect of bubble size on the flow pattern, gas holdup, residence time, and turbulence characteristics in the CZ was studied. The profiles of air content and bulk residence time for the symmetrical face under different bubble sizes are compared for the CZ (Fig. 5). The air content in the CZ is observed to be relatively constant regardless of the bubble size (Fig. 5& Fig. 7b), while the air content in the SZ decreases while bubble size increases. The increase of gas holdup with the decrease of bubble

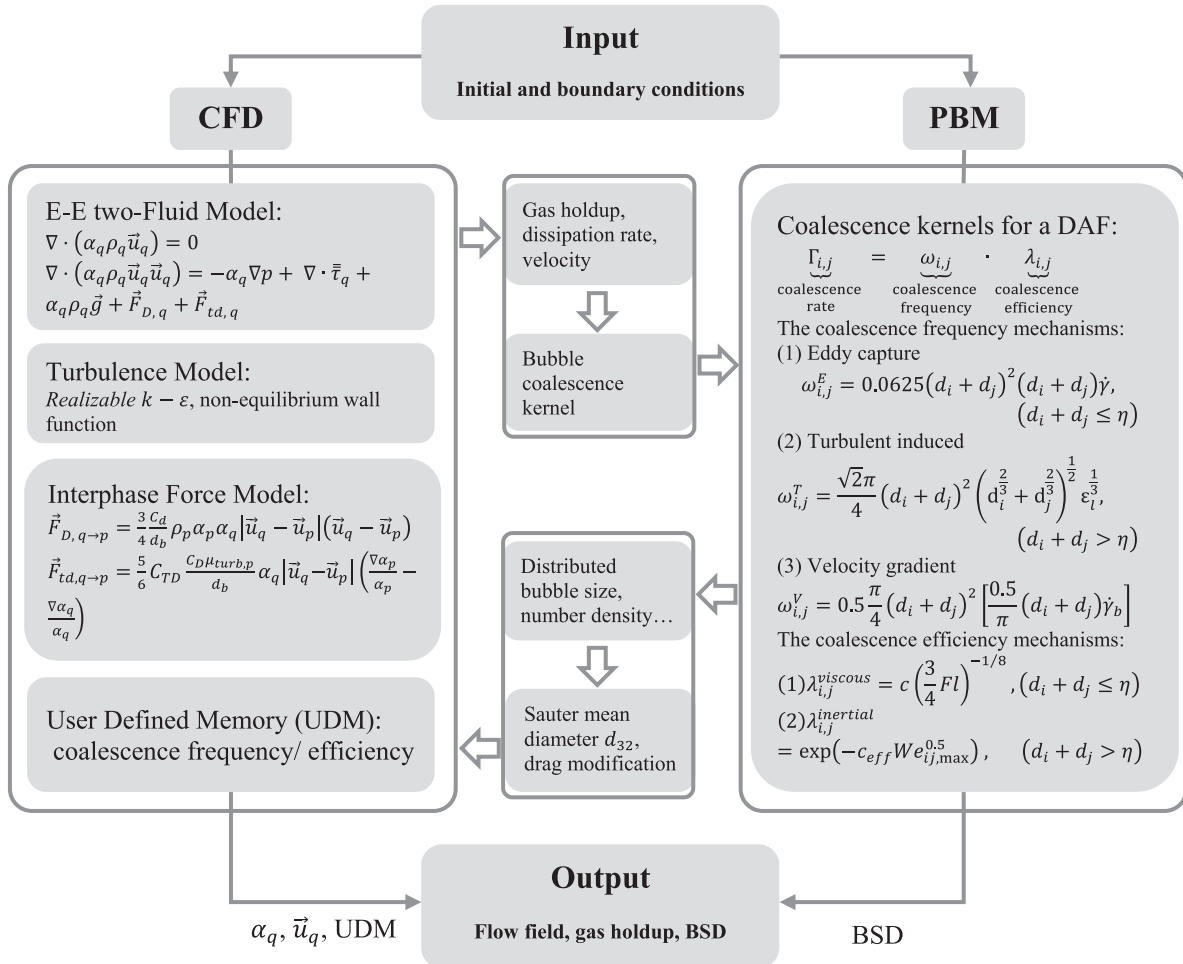


**Fig. 3.** A schematic diagram of the mechanism and coupling of the CFD-PBM model developed in this study.

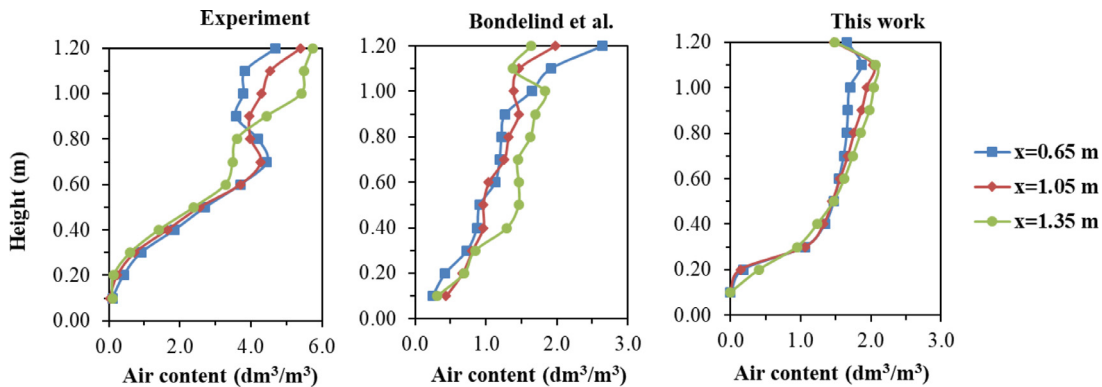


**Fig. 4.** The results of air content at the defined lines in the SZ obtained by CFD simulations in this study compared with the results from experimental measurements and CFD simulation work of Bondelind et al. [15].

size in the SZ is because that the smaller bubbles have a slower rise velocity than larger bubbles, and the mean flow and turbulence carry smaller bubbles to depth than larger bubbles [47]. The overall air content distribution in the DAF tank shown in Fig. 5a - Fig. 5e is related to the local mixing intensity presented in Fig. 5f, which shows the residence time profile. It can be seen that with a high mixing intensity and smaller RT in the CZ, the air content is rapidly and equally distributed in the CZ. While in the SZ, the air content tends to be high at locations where the mixing intensity is high.

As can be seen in Fig. 6, regardless of bubble size, a stratified flow occurred in the SZ for all bubble size, which is in accordance with the experimental measurements [25]. The microbubble plume is pushed toward the baffle by the injection nozzle and influent flow coming from the right, which then slides along the baffle. When it reaches the free surface, a portion of the flow moves toward the SZ and forms a stratified flow, while the remaining part rotates back inside the CZ and forms a circulation flow (Fig. 6). Flow circulation can be beneficial as it increases the local residence time and provides more collision opportunities among the microbubbles, flocs, and aggregates with very little

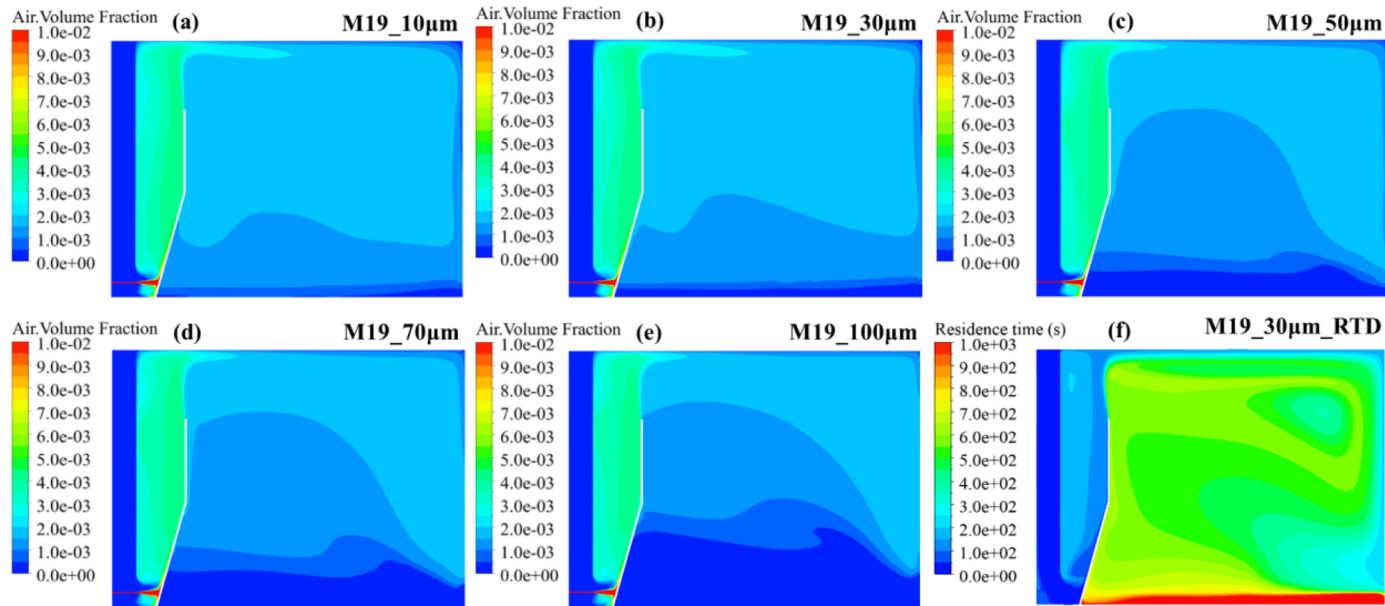


**Fig. 5.** CFD simulations of air content distribution on the symmetrical surface ( $y = 0.35$  m, M19) under different bubble size (a, b, c, d, e: 10, 30, 50, 70, and 100  $\mu\text{m}$ ), and residence time distribution under bubble size of 30  $\mu\text{m}$  (f).

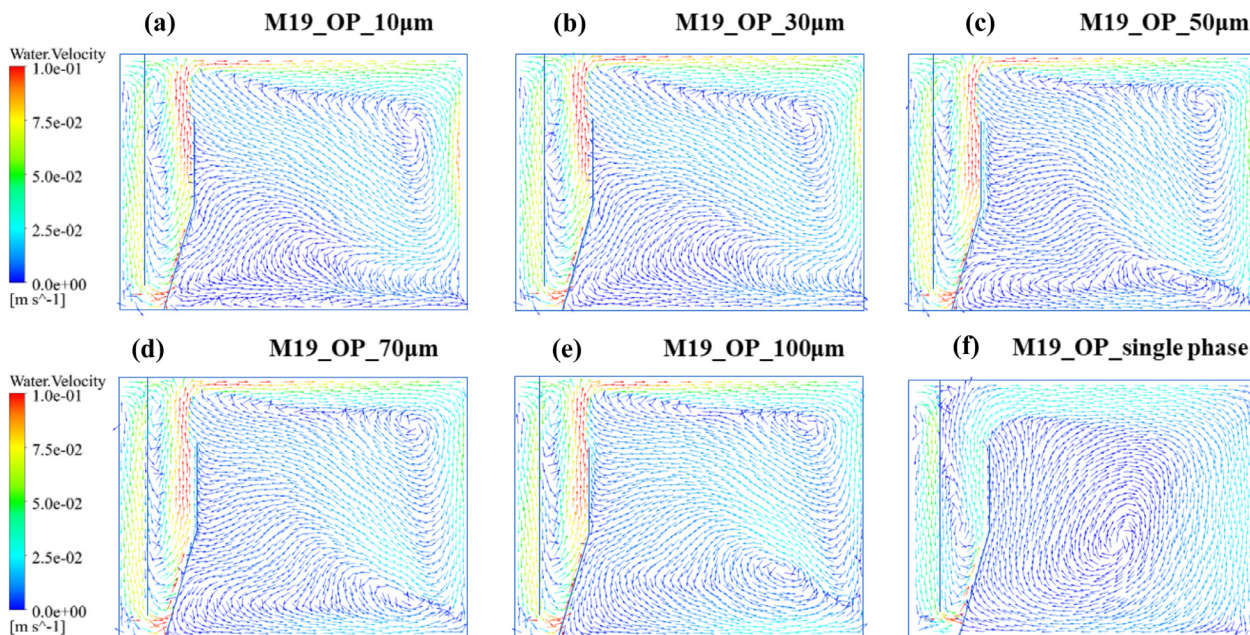


**Fig. 6.** CFD simulation results of velocity vectors under different bubble size ((a) to (e): 10, 30, 50, 70, and 100  $\mu\text{m}$ ) and ADV measurements (f) for flow pattern in the CZ of the DAF studied.

chance for floc detachment due to mild turbulence [48]. In the CZ, the gas and the liquid are being mixed intensely in a more restricted space, tending to be a more uniform distribution of the air content regardless of the bubble size.

As can be seen from the side view of the CZ in Fig. S2, the introduction of gas into the liquid increases the liquid rise velocity due to the decrease of the bulk viscosity and Buoyancy. After the microbubble plume reaches the free surface at the top, the fluid turns around. It descends along the walls on both sides, encountering another rising microbubble plume from the bottom, thereby forming multiple circulations (Fig. S2).

The fluid velocity flowing down the wall surface also increases when the bubble size increases, which leads to drawing less of the microbub-

ble plume into the circulation structure and thus weakens the circulation at the top. Correspondingly, it is observed that with different bubble sizes, different local residence time profiles are obtained (Fig. 7a). In general, the residence time at the top is higher than that at the bottom, where the fluid velocity is much higher. The creation of a strong rotation at the top tends to 'contain' the fluid, resulting in higher local residence time. As the bubble size increases, the circulation at the top weakens, and the residence time decreases accordingly (Fig. S2). As a result, when bubble size increases, the fluid tends to behave more like a plug flow due to the increase in Buoyancy and thus rising velocities (Fig. 7a). This partly explains why the scenarios with smaller bubble sizes (10  $\mu\text{m}$  and 30  $\mu\text{m}$ ) have a higher proportion of longer res-

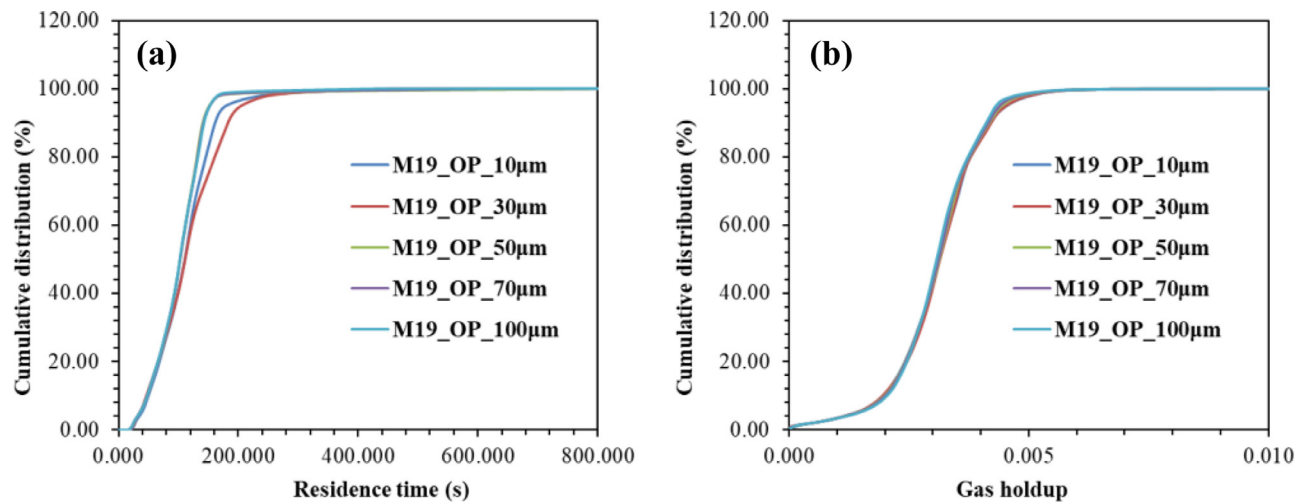


Fig. 7. The RN curves for the residence time (a) and RN curves for the gas holdup (b) in the CZ under different bubble sizes.

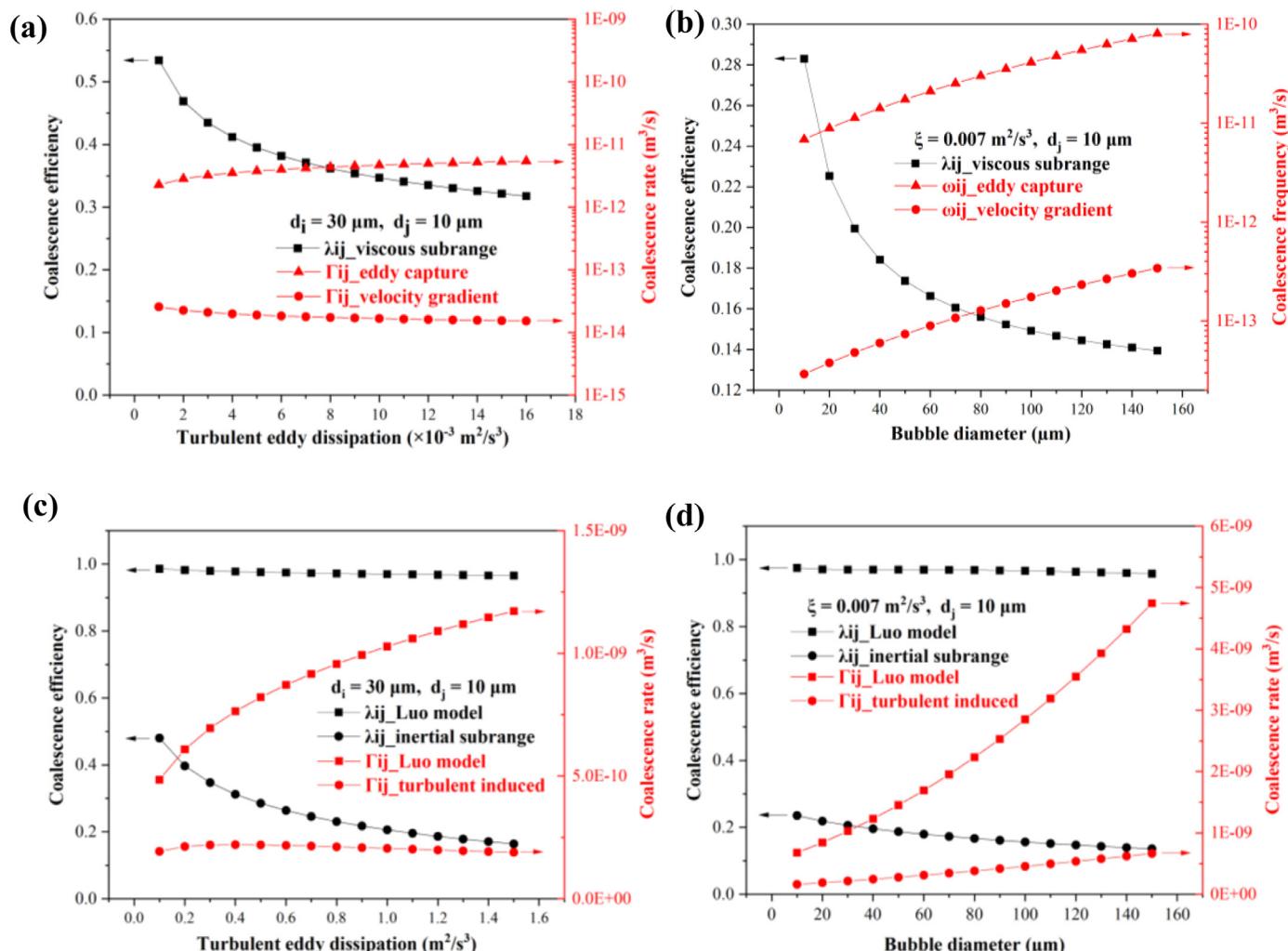
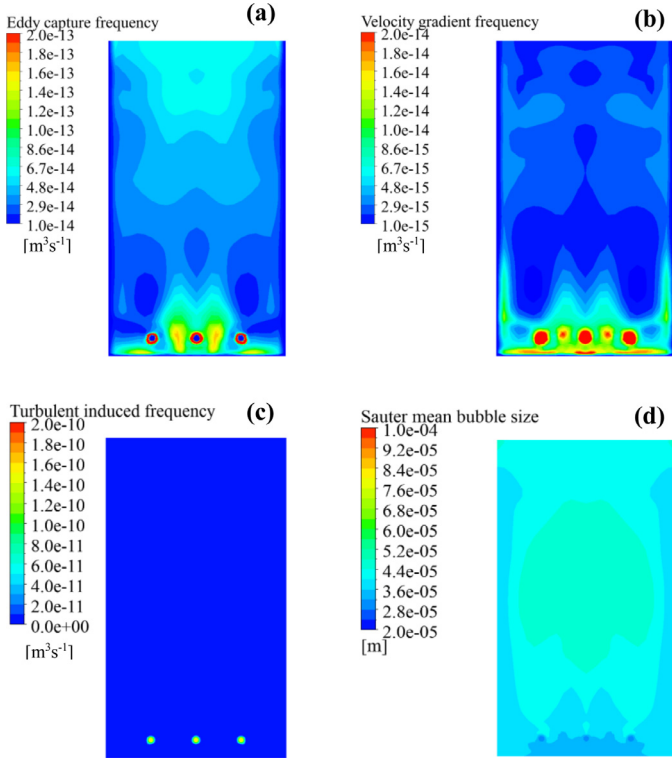


Fig. 8. The effect of turbulent eddy dissipation and bubble size on the collision rate under viscous shear flow (a, b) and under inertial subrange flow (c, d) in a typical DAF system.



**Fig. 9.** The visualization of the eddy capture frequency (a), velocity gradient frequency (b), turbulent induced frequency (c), and Sauter mean bubble size distribution (d) in the CZ for case M19.

idence time than the other three scenarios ( $50 \mu\text{m}$ ,  $70 \mu\text{m}$ , and  $100 \mu\text{m}$ ) (Fig. 7a).

In summary, the change of fluid dynamics such as the formation of rotation flows and residence time with various bubble sizes indicated that bubbles with a size of  $30 \mu\text{m}$  is favorable for the DAF system, which seems to be a sweet spot size for the DAF tank being studied, and is consistent with previous studies [16]. The fluid behavior is less favorable and remains almost unchanged when  $d_b$  equals or exceeds  $50 \mu\text{m}$  may due to the development of plug flow.

### 3.3. The contribution of different coalescence mechanisms to bubble size

The impact of turbulent eddy dissipation and bubble diameter on the collision frequency, coalescence efficiency and coalescence rate under different coalescence mechanisms is presented in Fig. 8. As expected, the coalescence efficiency ( $\lambda_{ij}$ ) decreases with both the increase in turbulent eddy dissipation (Fig. 8a, b) and bubble diameter (Fig. 8c, d) in different coalescence mechanisms (i.e., eddy capture, velocity gradient, and turbulent induced) [23,38]. Because the coalescence efficiency is inversely proportional to the drainage time, the time for removing the water entrapped between two colliding bubbles, bubbles need a longer time to undergo the drainage process between each other when the bubbles are large [36]. When turbulence is more intense, bubbles have less contact time to undergo coalescence, which also leads to a decrease in coalescence efficiency. In the default model provided by Fluent [49], all bubbles are arbitrarily assumed to be in the inertial subrange and have the same velocity as equalized eddies, which is not the case in the DAF system where the major bubble size is way smaller than the eddies [23]. As can be seen from Fig. 8, the Luo model yields an unreasonably high coalescence efficiency for microbubbles, which leads to a much higher coalescence rate compared to the coalescence kernel proposed in this work (Fig. 8c & 8d).

Even though the coalescence efficiency decrease for all scenarios, the coalescence rates grow with the increase both of bubble diameter and turbulent eddy dissipation (Fig. 8). This is attributed to the effect of the coalescence frequency, which increases exponentially with the bubble size and the turbulent eddy dissipation rate (Eq. (6), Eq. (14)). The eddy capture, which is one to two orders of magnitude higher in coalescence rate than that of the velocity gradient, is the dominant mechanism that drives the bubble coalescence for the viscous flow regime in the DAF system (Fig. 8a & 8b). For the flow under inertial subrange, eddy capture coalescence couldn't happen, and turbulent induced coalescence surpasses the other two mechanisms due to the significant high turbulent eddy dissipation (Fig. 8c & 8d). However, most of the volume of a DAF system usually has a very small turbulent intensity, and turbulent induced bubble coalescence is only expected to happen in the nozzle downstream (Fig. 9c).

### 3.4. Bubble size distribution in response to operation conditions

It can be seen from Fig. 9 that the bubble coalescence is closely related to the hydrodynamic characteristics. The coalescence frequencies are high in three major regions: around the nozzle inlet, on the flow path where the mixture fluid is sprayed from the nozzle inlet, and near the walls, which are in accordance with previous studies (Fig. 9a, b, and c) [23]. The turbulent eddy dissipation in these regions is high due to the high velocities and large velocity gradients. The bubble size distribution in the CZ of M18 predicted by CFD-PBM match the measurement data well under equivalent operation condition, implying that the three mechanisms chosen above to build a generic PBM are representative and sufficient for the prediction of DAF systems (Fig. 10a) [23].

When comparing Fig. 9a with 9b, it is found that the coalescence frequency induced by the eddy capture is one to two orders higher than that induced by the velocity gradient. In addition, the turbulent induced coalescence only occurs at the nozzle downstream as expected in Section 3.4 (Fig. 9c and Fig. 11). The bubble size in the nozzle downstream (Sauter diameter =  $\sim 31 \mu\text{m}$ ) didn't grow much compared to the nozzle inlet (Sauter diameter =  $\sim 30 \mu\text{m}$ ) due to the short period of time (Fig. 9d). The bubble size distribution curves of M18, M19, and M0 vary significantly between the nozzle inlet to the CZ. The bubble size distribution curves in the CZ of M18, M19 and M0 vary significantly from the nozzle inlet (Fig. 10). The curve of M19 slightly flattens and shifts to the right compared to M18, while the curve of M0 deviates significantly from that of the other two. The bubble coalescence leads to an increase in the average bubble size from  $30.0 \mu\text{m}$  at the inlet to  $40.0$ ,  $41.5$  and  $54.8 \mu\text{m}$  in the CZ for M18, M19 and M0 with a relative increase ratio of  $33.3\%$ ,  $38.3\%$ , and  $82.7\%$  compared to the nozzle inlet, respectively (Fig. 10a). The reason why M0 has the highest increase of bubble size in the CZ is that M0 has a lower recirculation rate and a higher air intake (Table 2), which gives bubble coalescence a higher contact time (Eq. (11) & Eq. (12)) and a higher coalescence frequency (Eq. (6)) simultaneously, especially at the nozzle downstream (Fig. S3). This implies that the turbulent induced coalescence can play a big role in bubble size, and turbulent in the nozzle downstream is better to be dissipated as fast as possible [50]. The smallest increase ratio for M18 can be explained by its lower air intake (only half of that of M19 and M0) and turbulent eddy dissipation (Table 2).

Compared with the volume fraction distribution, the number density distribution of the average bubble size is equally or even more important (Fig. 10c & Fig. 10d). The number density of case M0 is smaller for smaller bubbles ( $< 40 \mu\text{m}$ ) but is larger for larger bubbles ( $> 40 \mu\text{m}$ ) compared to that of case M19 in the CZ (Fig. 10c & Fig. S4). This is in line with the curve patterns of volume fraction distribution of the average bubble size (Fig. 10a). The CFD-PBM simulations indicate that even M18 has the smallest average bubble size, it still fails to provide the same level of amount of small bubbles compared to M0 and M19. Both M0 and M19 have a much larger number density than M18 in the whole spectrum of bubble size (Fig. 10c & Fig. S4) due to the lower air intake

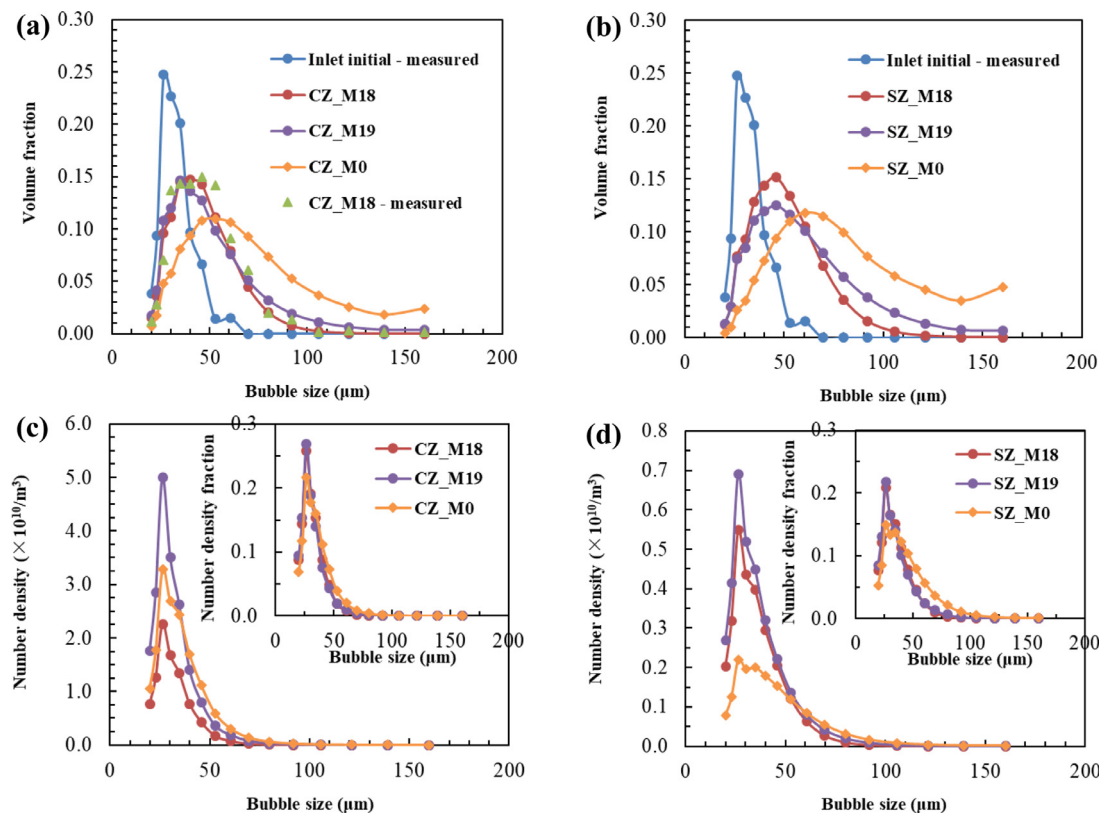


**Fig. 10.** Volume fractions distribution curves vs. bubble size in the CZ (a), in the SZ (b), and the corresponding bubble number density in the CZ (c) and in the SZ (d) for M18, M19 and M0.

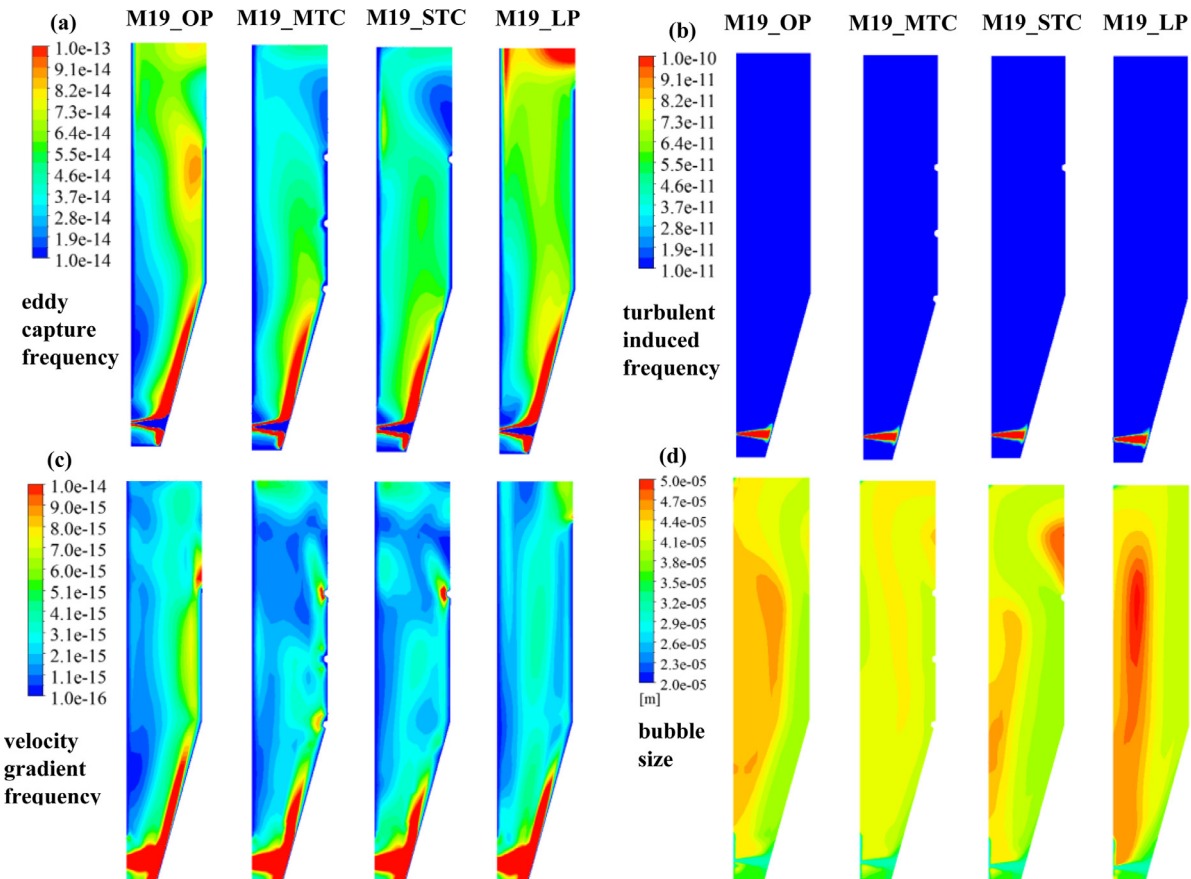


**Fig. 11.** Visualization of coalescence frequencies under different mechanisms (a ~ c) and the bubble size distribution (d) for different baffle configurations of case M19.

and thus lower gas holdup for M18 (Fig. S5). In addition, the bubble number density of M0 in the SZ decreased sharply compared to M18 and M19 due to the formation of larger bubbles (Fig. 10b & 10d). Because there is a trade-off between the coalescence frequency and coalescence efficiency (Fig. 8), the bubble number density can be manipulated by optimizing the recirculation ratio and gas volume fraction in the recirculation flow: increasing the recirculation rate (i.e., M19) is better than increasing the volume fraction in the smaller recirculated flow (i.e., M0) to achieve a higher bubble number density if the same amount of gas flow rate needs to be injected (Fig. 10).

Interestingly, even though the region with high turbulent eddy dissipation and velocity gradient have higher coalescence frequencies, the bubble sizes in these regions are smaller (Fig. 10). This is because the plume from the nozzle flows through these regions first, but the bubbles will continue to grow in other regions. This indicates that the local residence time in the CZ is also crucial for bubble size growth. Increasing the CZ residence time ( $t_{cz}$ ) improves the CZ performance only if the  $t_{cz}$  is not too large to generate over large bubbles due to coalescence. The effect of  $t_{cz}$  on the bubble coalescence revealed here explains why in practice, the CZ residence time lies between 1.0 and 2.5 min for design flow conditions, and an optimal residence time depends on the specific operation and configuration [6].

The bubbles continue growing in the SZ but at a much slower rate due to the dramatic decrease of flow velocity and turbulent intensity, giving M18, M19 and M0 an average bubble size of 41.1, 43.6, and 57.5  $\mu\text{m}$  in the SZ with a relative increase ratio of 2.8%, 5.1%, and 4.9% compared to that of the CZ, respectively (Fig. 10a & 10b). This finding is in accordance with the experimental results in a measurement performed at the Graincliffe Water Treatment Works, in which the bubble size distribution at a depth of 0.2 m at the CZ and SZ didn't seem to differ when the surface loading was identical to this study [47].

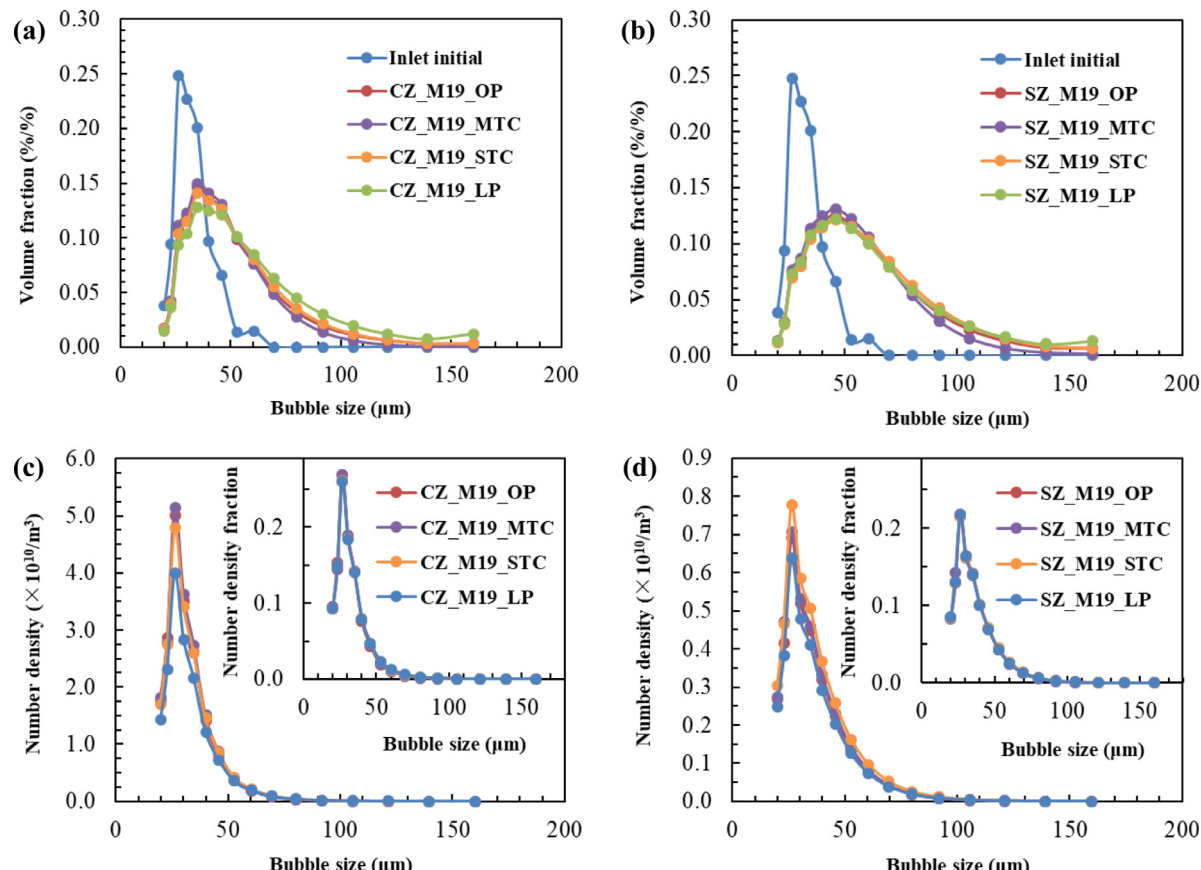


**Fig. 12.** Bubble volume fractions distribution curves vs. bubble size in the CZ (a), in the SZ (b), and the corresponding bubble number density in the CZ (c) and the SZ (d) for M19 for different baffles.

### 3.5. Bubble size distribution in response to the baffle configurations

While the turbulent induced coalescence doesn't seem to make a change (Fig. 11b), the bubble coalescence frequencies due to eddy capture and velocity gradient vary in different baffle configurations (Fig. 11a & 11c). The magnitude order of overall coalescence frequencies appears to be MTC < STC < OP < LP (Fig. S5), which leads to a Sauter mean bubble size order of LP>OP>STC>MTC (Fig. 11d).

The transverse corrugate in MTC and STC plays an important role in equalizing the distribution of eddy capture induced and velocity gradient coalescence efficiency. The high coalescence efficiency regions largely presented near the free surface and the middle region of the LP baffle disappears in the MTC and STC baffle (Fig. 11a). This could be the main reason why the bubble size distribution curve for the MTC baffle narrows and shift to the left from the LP baffle (Fig. 12a & Fig. 12b). The larger bubble for the MTC baffle drops significantly while the smaller bubble number density increases (Fig. 12c & Fig. 12d). However, the MTC baffle generates multiple circulations resulting in a slower gas replenishment and higher bubble growth in these regions, which leads to the least steep gas holdup curve and may offset the advantage of its lower coalescence rate. Instead, the STC baffle seems to be the most prominent configuration as it maintains the highest gas holdup in the CZ and the SZ (Fig. S6 & S7), implying that the CZ efficiency can be improved by increasing turbulence and creating a rotational flow to a critical point while avoiding generating excessive large bubbles. Increasing the height of the baffle to a level that generates high eddy capture coalescence doesn't seem to be a wise choice (Fig. S6). Compared to other baffles, the LP baffle generates an obvious larger eddy-capture induced coalescence at the top of the CZ due to the intense mixing that appears at this region, which was also observed by a PIV measurement [12]. As can be seen for the LP baffle, the bubble number density is much less

than the other three (Fig. 12), and the gas holdup is also the lowest due to the generation of over large bubbles, which are expected to escape from the system more quickly (Fig. 12& Fig. S6).

As shown in this Section and Section 3.4, the CFD-PBM model allows a better understanding of the fundamentals and explaining the phenomenon occurring in the DAF system. It enables simulating many different scenarios of different factor combinations to establish synergy with the aim of obtaining a larger volume fraction and a larger number density of the desired bubble size. The CFD-PBM simulations show that the baffle configuration plays a role in bubble size distribution and gas holdup. Considering both the bubble number density and gas holdup, the STC baffle seems to be an optimal configuration compared to the original one in this DAF system. Even so, it is not a trivial task to reach a conclusion on an optimal solution even without the consideration of the particle phase in this study. But such optimizations are even nearly impossible to be achieved by using only CFD with the mono bubble size assumption (Fig. 5). Further investigation with a complete three-phase model and experimental efforts are needed in the future.

#### 4. Conclusions

A generic CFD-PBM model was developed for DAF systems and used for operational and structural optimization for a pilot DAF. CFD-PBM simulations showed that the eddy capture mechanism dominated the microbubble coalescence in most of the volume in the CZ, while the velocity gradient mechanism and turbulent induced mechanism also play a key role in regions with drastic flow transition and in the nozzle downstream, respectively. The CFD-PBM model developed in this study increases the CFD prediction power by giving the bubble size distribution information. The optimal operation and design for the studied DAF system were obtained: instead of increasing the volume fraction of the recirculated gas ( $M_0$ ), it is better to increase the recirculation rate to shorten the turbulent coalescence time in the nozzle downstream ( $M_{19}$ ), thereby reducing the total coalescence rate as revealed by CFD-PBM; the STC baffle seems to be an optimal configuration in the studied scenarios considering the bubble number density and gas holdup.

#### Declaration of Competing Interest

The authors declare that they have no known competing financial interests or personal relationships that could have appeared to influence the work reported in this paper.

#### Acknowledgments

This work is supported by a Marie Skłodowska-Curie Individual Fellowship of the European Commission's Horizon 2020 Programme (841521).

#### Supplementary materials

Supplementary material associated with this article can be found, in the online version, at doi:10.1016/j.cej.2021.100131.

#### References

- [1] European Commision, The EU Water Framework Directive, 2020 [https://ec.europa.eu/environment/water/index\\_en.htm](https://ec.europa.eu/environment/water/index_en.htm).
- [2] K. Satpathy, U. Rehman, B. Cools, L. Verdickt, G. Peleman, I. Nopens, CFD-Based process optimization of a dissolved air flotation system for drinking water production, *Water Sci. Technol.* (2020) 1–14, doi:10.2166/wst.2020.028.
- [3] S. Shrestha, J. Kulandaivelu, K. Sharma, G. Jiang, Z. Yuan, Effects of dosing iron- and alum-containing waterworks sludge on sulfide and phosphate removal in a pilot sewer, *Chem. Eng. J.* 387 (2020) 124073, doi:10.1016/j.cej.2020.124073.
- [4] P. Palaniandy, M.N. Adlan, H.A. Aziz, M.F. Murshed, Application of dissolved air flotation (DAF) in semi-aerobic leachate treatment, *Chem. Eng. J.* 157 (2010) 316–322, doi:10.1016/j.cej.2009.11.005.
- [5] C. Cagnetta, B. Saerens, F.A. Meerburg, S.O. Decru, E. Broeders, W. Menkveld, T.G.L. Vandekerckhove, J. De Vrieze, S.E. Vlaeminck, A.R.D. Verliefde, B. De Gusseme, M. Weemaes, K. Rabaey, High-rate activated sludge systems combined with dissolved air flotation enable effective organics removal and recovery, *Bioresour. Technol.* 291 (2019) 121833, doi:10.1016/j.biortech.2019.121833.
- [6] J. Haarhoff, J.K. Edzwald, Dissolved air flotation modelling: insights and shortcomings, *J. Water Supply Res. Technol. - AQUA* 53 (2004) 127–150, doi:10.2166/aqua.2004.0012.
- [7] O. Levenspiel, *Chemical Reaction Engineering*, John Wiley & Sons, 1999.
- [8] A.R. Shawwa, D.W. Smith, Hydrodynamic characterization in dissolved air flotation (DAF) contact zone, *Water Sci. Technol.* 38 (1998) 245–252, doi:10.1016/S0273-1223(98)00585-X.
- [9] J.K. Edzwald, Developments of high rate dissolved air flotation for drinking water treatment, *J. Water Supply Res. Technol.* 56 (2007) 399, doi:10.2166/aqua.2007.013.
- [10] J.K. Edzwald, Principles and applications of dissolved air flotation, *Water Sci. Technol.* 31 (1995) 1–23, doi:10.1016/0273-1223(95)00200-7.
- [11] J.K. Edzwald, Dissolved air flotation and me, *Water Res.* 44 (2010) 2077–2106, doi:10.1016/j.watres.2009.12.040.
- [12] V.R. Fanaie, M. Khadiani, T. Ayres, Effects of internal geometry on hydrodynamics of dissolved air flotation (DAF) tank: an experimental study using particle image velocimetry (PIV), *Colloids Surfaces A Physicochem. Eng. Asp.* 575 (2019) 382–390, doi:10.1016/j.colsurfa.2019.05.027.
- [13] J.P. Rodrigues, R. Bétega, Evaluation of multiphase CFD models for Dissolved Air Flotation (DAF) process, *Colloids Surfaces A Physicochem. Eng. Asp.* 539 (2018) 116–123, doi:10.1016/j.colsurfa.2017.12.015.
- [14] B. Lakghomi, Y. Lawryshyn, R. Hofmann, A model of particle removal in a dissolved air flotation tank: importance of stratified flow and bubble size, *Water Res.* 68 (2015) 262–272, doi:10.1016/j.watres.2014.09.053.
- [15] M. Bondelind, S. Sasic, M. Kostoglou, L. Bergdahl, T.J.R. Pettersson, Single- and two-phase numerical models of Dissolved Air Flotation: comparison of 2D and 3D simulations, *Colloids Surfaces A Physicochem. Eng. Asp.* 365 (2010) 137–144, doi:10.1016/j.colsurfa.2010.02.035.
- [16] A. Chen, Z. Wang, J. Yang, Influence of bubble size on the fluid dynamic behavior of a DAF tank: a 3D numerical investigation, *Colloids Surfaces A Physicochem. Eng. Asp.* 495 (2016) 200–207, doi:10.1016/j.colsurfa.2015.10.039.
- [17] K. Satpathy, U. Rehman, B. Cools, L. Verdickt, G. Peleman, I. Nopens, CFD-Based process optimization of a dissolved Air flotation system for drinking water production, *Water Sci. Technol.* (2020) 1–14, doi:10.2166/wst.2020.028.
- [18] I. Nopens, E. Torfs, J. Ducoste, P.A. Vanrolleghem, K.V. Gernaey, Population balance models: a useful complementary modelling framework for future WWTP modelling, *Water Sci. Technol.* 71 (2015) 159–167, doi:10.2166/wst.2014.500.
- [19] M. Basavarajappa, S. Miskovic, Investigation of gas dispersion characteristics in stirred tank and flotation cell using a corrected CFD-PBM quadrature-based moment method approach, *Miner. Eng.* 95 (2016) 161–184, doi:10.1016/j.mineng.2016.06.026.
- [20] G. Wang, L. Ge, S. Mitra, G.M. Evans, J.B. Joshi, S. Chen, A review of CFD modelling studies on the flotation process, *Miner. Eng.* 127 (2018) 153–177, doi:10.1016/j.mineng.2018.08.019.
- [21] A.R. Sarhan, J. Naser, G. Brooks, CFD simulation on influence of suspended solid particles on bubbles' coalescence rate in flotation cell, *Int. J. Miner. Process.* 146 (2016) 54–64, doi:10.1016/j.minpro.2015.11.014.
- [22] A.R. Sarhan, J. Naser, G. Brooks, CFD analysis of solid particles properties effect in three-phase flotation column, *Sep. Purif. Technol.* 185 (2017) 1–9, doi:10.1016/j.seppur.2017.04.042.
- [23] A. Chen, W. Yang, S. Geng, F. Gao, T. He, Z. Wang, Q. Huang, Modeling of Microbubble Flow and Coalescence Behavior in the Contact Zone of a Dissolved Air Flotation Tank Using a Computational Fluid Dynamics-Population Balance Model, *Ind. Eng. Chem. Res.* 58 (2019) 16989–17000, doi:10.1021/acs.iecr.9b03604.
- [24] J.P. Rodrigues, J.N.M. Batista, R. Bétega, Application of population balance equations and interaction models in CFD simulation of the bubble distribution in dissolved air flotation, *Colloids Surfaces A Physicochem. Eng. Asp.* 577 (2019) 723–732, doi:10.1016/j.colsurfa.2019.06.032.
- [25] M. Lundh, L. Jönsson, J. Dahlquist, The influence of contact zone configuration on the flow structure in a dissolved air flotation pilot plant, *Water Res.* 36 (2002) 1585–1595, doi:10.1016/S0043-1354(01)00357-8.
- [26] M. Lundh, L. Jönsson, J. Dahlquist, Experimental studies of the fluid dynamics in the separation zone in dissolved air flotation, *Water Res.* 34 (2000) 21–30, doi:10.1016/S0043-1354(99)00136-0.
- [27] M. Yang, D. Yu, M. Liu, L. Zheng, X. Zheng, Y. Wei, F. Wang, Y. Fan, Optimization of MBR hydrodynamics for cake layer fouling control through CFD simulation and RSM design, *Bioresour. Technol.* 227 (2016) 102–111, doi:10.1016/j.biortech.2016.12.027.
- [28] A.D. Burns, T. Frank, I. Hamill, J.M. Shi, The Favre averaged drag model for turbulent dispersion in Eulerian multi-phase flows, 5th Int. Conf. Multiph. Flow. (2004) 1–17 [http://www.drthfrank.de/publications/2004/Burns\\_Frank\\_ICMF\\_2004\\_final.pdf](http://www.drthfrank.de/publications/2004/Burns_Frank_ICMF_2004_final.pdf).
- [29] U. Rehman, *Next Generation Bioreactor Models For Wastewater Treatment Systems By Means of Detailed Combined Modelling of Mixing and Biokinetics PhD thesis*, 2016.
- [30] N. Jourdan, T. Neveux, O. Potier, M. Kanniche, J. Wicks, I. Nopens, U. Rehman, Y. Le Moulec, Compartmental Modelling in chemical engineering: a critical review, *Chem. Eng. Sci.* 210 (2019) 115196, doi:10.1016/j.ces.2019.115196.

- [31] T. Wang, J. Wang, Y. Jin, A novel theoretical breakup kernel function for bubbles /droplets in a turbulent flow, *Chem. Eng. Sci.* 58 (2003) 4629–4637, doi:[10.1016/j.ces.2003.07.009](https://doi.org/10.1016/j.ces.2003.07.009).
- [32] M.J. Prince, H.W. Blanch, Bubble Coalescence and Break-Up in Air-Sparged Bubble Columns, *Sci. Eng. Princ. Appl.* 36 (1990) 1485–1499, doi:[10.1016/b978-0-08-025383-1.50085-0](https://doi.org/10.1016/b978-0-08-025383-1.50085-0).
- [33] T. Wang, J. Wang, Y. Jin, Population balance model for gas - Liquid flows: influence of bubble coalescence and breakup models, *Ind. Eng. Chem. Res.* 44 (2005) 7540–7549, doi:[10.1021/ie0489002](https://doi.org/10.1021/ie0489002).
- [34] R. Shinnar, J.M. Church, Predicting Particle Size in Agitated Dispersions, 52 (1960) 1–4.
- [35] Y. Liao, D. Lucas, A literature review on mechanisms and models for the coalescence process of fluid particles, *Chem. Eng. Sci.* 65 (2010) 2851–2864, doi:[10.1016/j.ces.2010.02.020](https://doi.org/10.1016/j.ces.2010.02.020).
- [36] A.K. Chesters, Modelling of coalescence processes in fluid-liquid dispersions. A review of current understanding, *Chem. Eng. Res. Des.* 69 (1991) 259–227.
- [37] D. Colella, D. Vinci, R. Bagatin, M. Masi, E.A. Bakr, A study on coalescence and breakage mechanisms in three different bubble columns, *Chem. Eng. Sci.* 54 (1999) 4767–4777.
- [38] Y. Liao, R. Rzebak, D. Lucas, E. Krepper, Baseline closure model for dispersed bubbly flow: bubble coalescence and breakup, *Chem. Eng. Sci.* 122 (2015) 336–349, doi:[10.1016/j.ces.2014.09.042](https://doi.org/10.1016/j.ces.2014.09.042).
- [39] X. Guo, C. Chen, Simulating the impacts of internals on gas-liquid hydrodynamics of bubble column, *Chem. Eng. Sci.* 174 (2017) 311–325, doi:[10.1016/j.ces.2017.09.004](https://doi.org/10.1016/j.ces.2017.09.004).
- [40] I.U. Vakarelski, R. Manica, E.Q. Li, E.S. Basheva, D.Y.C. Chan, S.T. Thoroddsen, Coalescence Dynamics of Mobile and Immobile Fluid Interfaces, *Langmuir* 34 (2018) 2096–2108, doi:[10.1021/acs.langmuir.7b04106](https://doi.org/10.1021/acs.langmuir.7b04106).
- [41] ANSYSANSYS FLUENT Population Balance Module Manual, ANSYS, Inc., 2012.
- [42] M.J. Hounslow, R.L. Ryall, V.R. Marshall, A discretized population balance for nucleation, growth, and aggregation, *AICHE J.* 34 (1988) 1821–1832, doi:[10.1002/aic.690341108](https://doi.org/10.1002/aic.690341108).
- [43] D. Ramkrishna, Population Balances Theory and Applications to Particulate Systems in Engineering Doraiswami, Academic Press, San Diego, 2000, doi:[10.1016/b978-044452237-5.50012-6](https://doi.org/10.1016/b978-044452237-5.50012-6).
- [44] D.L. Marchisio, R.D. Vigil, R.O. Fox, Quadrature method of moments for aggregation-breakage processes, *J. Colloid Interface Sci.* 258 (2003) 322–334, doi:[10.1016/S0021-9797\(02\)00054-1](https://doi.org/10.1016/S0021-9797(02)00054-1).
- [45] M. Lundh, L. Jönsson, J. Dahlquist, The flow structure in the separation zone of a DAF pilot plant and the relation with bubble concentration, *Water Sci. Technol.* 43 (2001) 185–194.
- [46] S. Buethorn, Experimental and Numerical Investigation of the Hydrodynamics of Microfiltration Processes Using a Multi-Scale Approach (No. RWTH-CONV-107810), Lehrstuhl für Chemische Verfahrenstechnik und Institut für Verfahrenstechnik, 2011.
- [47] D.M. Leppinen, S.B. Dalziel, Bubble size distribution in dissolved air flotation tanks, *J. Water Supply Res. Technol. - AQUA.* 53 (2004) 531–543, doi:[10.2166/aqua.2004.0042](https://doi.org/10.2166/aqua.2004.0042).
- [48] K.H. Lee, H. Kim, J.W. KuK, J.D. Chung, S. Park, E.E. Kwon, Micro-bubble flow simulation of dissolved air flotation process for water treatment using computational fluid dynamics technique, *Environ. Pollut.* (2019) 112050, doi:[10.1016/j.envpol.2019.01.011](https://doi.org/10.1016/j.envpol.2019.01.011).
- [49] H. Luo, Coalescence, Breakup and Liquid Circulation in Bubble Column Reactors, the Norwegian Institute of Technology, 1993.
- [50] S.E. de Rijk, G. Jaap H.J.M. aivan der, J.G. den Blanken, Bubble size in flotation thickening, *Water Res* 28 (1994) 465–473, doi:[10.1016/0043-1354\(94\)90284-4](https://doi.org/10.1016/0043-1354(94)90284-4).